achieved for method B of Section IV-B. The total reduction rate when method B is applied on top of method A is shown in columns 5, 9, and 13. The proposed compaction technique is very effective since the total reduction rates are between 70% and 84% for all circuits. The last row of Table IV reports the average reduction rates for all listed circuits. Average time performance (in CPU seconds) of each circuit, demonstrating the proposed scheme's efficiency, is given in column 14.

VI. Conclusion

This paper presents a novel methodology for efficient generation of transition-fault test functions for high-quality tests. The obtained experimental results demonstrate that the examined test functions can be generated quickly and with reasonable memory requirements. They also show that in many cases, only a small percentage of the faults for the examined problem can have high-quality tests. Test-set enhancement techniques that can be applied to produce better quality test sets, given a set of transition-fault test functions, are also presented. It is shown how test functions are advantageous for a variety of reasons, among which are compact test generation and nonenumerative path sensitization of many critical paths.

References

[1] D. Bhattacharya, P. Agrawal, and V. D. Agrawal, "Test pattern generation for path delay faults using binary decision diagrams," *IEEE Trans. Comput.*, vol. 44, no. 3, pp. 434–447, Mar. 1995.

[2] R. Bryant, "Graph-based algorithms for Boolean function manipulation," *IEEE Trans. Comput.*, vol. C-35, no. 8, pp. 677–691, Aug. 1986.

[3] K. T. Cheng and H. C. Chen, "Classification and identification of nonrobust untestable path delay faults," *IEEE Trans. Comput.-Aided Design Integr. Circuits Syst.*, vol. 15, no. 8, pp. 845–853, Aug. 1996.

[4] M. A. Gharaybeh, M. L. Bushnell, and V. D. Agrawal, "The path-status graph with application to delay fault simulation," *IEEE Trans. Comput.-Aided Design Integr. Circuits Syst.*, vol. 17, no. 4, pp. 324–332, Apr. 1998.

[5] H. Hulgaard, P. F. Williams, and H. R. Andersen, "Equivalence checking of combinational circuits using Boolean expression diagrams," *IEEE Trans. Comput.-Aided Design Integr. Circuits Syst.*, vol. 18, no. 7, pp. 903–917, Jul. 1999.

[6] D. A. Kirkpatrick and A. L. Sangiovanni-Vincentelli, "Digital sensitivity: Predicting signal interaction using functional analysis," in *Proc. ICCAD*, Nov. 1996, pp. 536–541.

[7] H. Konuk, "On invalidation mechanisms for non-robust delay tests," in *Proc. ITC*, Oct. 2000, pp. 393–399.

[8] Y. Levendel and P. R. Menon, "Transition faults in combinational circuits: Input transition test generation and fault simulation," in *Proc. FTCS*, Jul. 1986, pp. 278–283.

[9] C. J. Lin and S. M. Reddy, "On delay fault testing in logic circuits," *IEEE Trans. Comput.-Aided Design Integr. Circuits Syst.*, vol. CAD-6, no. 5, pp. 694–703, Sep. 1987.

[10] M. K. Michael and S. Tragoudas, "Functions-based compact test pattern generation for path delay faults," *IEEE Trans. Very Large Scale Integr. (VLSI) Syst.*, vol. 13, no. 8, pp. 996–1001, Aug. 2005.

[11] M. K. Michael, T. Haniotakis, and S. Tragoudas, "A unified framework for generating all propagation functions for logic errors and events," *IEEE Trans. Comput.-Aided Design Integr. Circuits Syst.*, vol. 23, no. 6, pp. 980–986, Jun. 2004.

[12] I. Pomeranz and S. M. Reddy, "On n-detection test sets and variable n-detection test sets for transition faults," *IEEE Trans. Comput.-Aided Design Integr. Circuits Syst.*, vol. 19, no. 3, pp. 372–383, Mar. 2000.

[13] A. K. Pramanick and S. M. Reddy, "On the detection of delay faults," in *Proc. ITC*, Sep. 1988, pp. 845–856.

[14] M. H. Schulz and F. Brglez, "Accelerated transition fault simulation," in *Proc. DAC*, Jun. 1987, pp. 237–243.

[15] Y. Shao, I. Pomeranz, and S. M. Reddy, "On generating high quality tests for transition faults," in *Proc. 11th ATS*, 2002, pp. 1–8.

[16] G. L. Smith, "Model for delay faults based upon paths," in *Proc. ITC*, Nov. 1985, pp. 342–349.

[17] F. Somenzi, *CUDD: CU Decision Diagram Packag*. Boulder, CO: Dept. ECE, Univ. Colorado, 1999.

[18] C.-W. Tseng and E.-J. McCluskey, "Multiple-output propagation transition fault test," in *Proc. ITC*, 2001, pp. 358–366.

[19] K. Yang, K. T. Cheng, and L. C. Wang, "TranGen: A SAT-based ATPG for path-oriented transition faults," in *Proc. ASP-DAC*, 2004, pp. 92–97.

Efficient Direct Boundary Element Method for Resistance Extraction of Substrate With Arbitrary Doping Profile

Xiren Wang, Wenjian Yu, and Zeyi Wang

***Abstract*—It is important to model the substrate coupling for mixed-signal or RF circuit designs. In this paper, a direct boundary element method (DBEM) and related efficient techniques are presented to calculate the coupling resistances for three-dimensional substrate structure. First, a nonuniform meshing scheme is presented to reduce boundary elements while preserving accuracy. Then, the unknowns on top medium surface are removed from the discretized linear system of DBEM with a matrix reduction technique. The third technique is applying the quasi-multiple medium idea (W. Yu, Z. Wang, and J. Gu, "Fast capacitance extraction of actual 3-D VLSI interconnects using quasi-multiple medium accelerated BEM," *IEEE Trans. Microwave Theory Tech.*, vol. 51, no. 1, pp. 109–199, Jan. 2003), which greatly reduces the expense of matrix reduction and makes the final coefficient matrix much sparser. With these proposed techniques, the linear equation system is largely condensed and sparsified and then solved with a preconditioned generalized minimum residual solver for multiple right-hand sides to get the whole resistance matrix. Numerical experiments on typical substrates with various doping profiles show the high accuracy of the DBEM-based method. The authors also compared the DBEM method with the Green's function methods accelerated by discrete cosine transform or eigendecomposition techniques. The results show that the DBEM-based method is several times or tens of times faster than the other two. At the same time, the DBEM method has no difficulty in handling substrates with more complex than stratified doping profiles, which is a large advantage over the existing methods.**

***Index Terms*—Direct boundary element methods (DBEMs), efficient extraction of resistance, substrates with arbitrary doping profiles.**

I. Introduction

There are currently increasing demands for high-integration circuits [1]. High-speed digital blocks and highly sensitive analog blocks are often built on a common substrate, which is especially true for system-on-a-chip, mixed-signal, or RF applications. The high integration brings some advantages, e.g., low-power dissipation, low cost, etc. [2]. However, the commonly used Si substrate transmits current noises from digital components to sensitive analog components, which impacts the latter's performance severely. Therefore, the accurate and fast modeling of the substrate coupling becomes very important.

At frequency of several gigahertz (GHz), a substrate behaves mainly resistively [3]. Therefore, the substrate coupling is often modeled with resistances connecting the contacts on its top surface. The substrate resistances can be calculated with a device simulator, such as MEDICI.

Manuscript received July 8, 2005; revised November 24, 2005 and January 6, 2006. This work was supported by the China National Science Foundation under Grant 60401010. This paper was recommended by Associate Editor L. M. Silveira.

The authors are with the Electronic Design Automation (EDA) Lab, Department Computer Science and Technology, Tsinghua University, Beijing 100084, China (e-mail: xirenwang99@gmail.com; yu-wj@tsinghua.edu.cn; wangzy@tsinghua.edu.cn).

Digital Object Identifier 10.1109/TCAD.2006.882487

Because complex physical effects, such as drift and diffusion, are involved, the device simulator runs very slowly [2]. A practical method may be the curve fitting with data obtained from device simulator or measurement. Although this approach is fast in some sense, their application is very limited [2]. Other kinds of methods are based on analytical formulas [4], which are efficient for some special cases, but hardly suitable for general structures. A lot of numerical methods are also utilized to calculate the substrate resistance with high accuracy. They can be classified into the finite-element method (FEM), finite difference method (FDM) [5], and the method of Green's function [also called boundary element method (BEM)] [2], [3], [6]–[10]. The FEM and FDM, with discretization of the whole three-dimensional (3-D) substrate volume, produce a large coefficient matrix, which limits the size of problem that they can handle. The methods based on the Green's function, such as those in [2], [3], [6]–[10], only discretize the contact surfaces, therefore employs the fewest variables. However, for the multilayered structure, the Green's function is composed of several infinite series, which converge very slowly. In [7], a numerically stable method was proposed to calculate the Green's function with discrete cosine transform (DCT) for acceleration. However, it is not actually stable, and a further remedy was presented in [8]. It should be pointed out that these Green's function-based methods are limited to the multilayer structure where each layer has a uniform resistivity. For more complex structures such as those containing lateral resistivity variations, the corresponding Green's function can hardly be deduced [9], [11]. One way to deal with the lateral variation is to use a combined boundary element and FEM [11], where the top part of substrate with inhomogeneous material is discretized with FEM mesh. Therefore, this method still requires larger computational resources.

In fact, there are lots of realistic substrates with layout-dependent doping profiles, such as the oxide wells, trenches, sinkers, buried diffusions, etc. [12]. There are also some special structures like Faraday shields and junction shields [13] for noise reduction, which are actually buried components with different resistivity. For these nonstratified substrates, the derivation of the Green's function becomes very difficult or even impossible. On the other hand, neglecting the special components simply may induce large error for the simulation of the state-of-the-art technologies, such as RF CMOS [12].

Different from the Green's function-based method, there is another kind of boundary integral method called direct BEM (DBEM) [14]. The DBEM obtains the direct boundary integral equation (BIE) by adopting Green's identity and using the free-space Green's function as weighting function [14]. Therefore, it avoids the difficulties of deducing the structure-dependent Green's function and also employs much fewer variables than the FDM or FEM. Recently, the DBEM has been successfully applied to capacitance and resistance extraction for various interconnect structures [15], [16].

In this paper, the DBEM is introduced to substrate resistance extraction, along with several efficient techniques. First, a nonuniform boundary element partition scheme is presented as a basis of efficient DBEM simulation. Second, some inessential unknowns are removed from the discretized linear system of DBEM using a matrix reduction technique, which produces a smaller order of linear system without loss of accuracy. Finally, the technique called quasi-multiple medium (QMM) innovated for capacitance extraction [15] is used to make the coefficient matrix much sparser, so as to reduce the expense of matrix reduction and final equation solution greatly. Numerical experiments are carried out to illustrate the accuracy and efficiency of our method based on DBEM. Its results are compared with DCT-accelerated Green's function method and the eigendecomposition-based method in [2] and an analytical integration method in [10]. The results of Raphael [17] and IE3-D [10] are also given for reference. Numerical results show that our method is superior to the methods in [2] and [10] in CPU time and has speedup of several hundreds to Raphael and IE3-D while preserving high accuracy. Especially, our method is applied to a substrate structure with lateral resistivity variation to demonstrate its versatility.

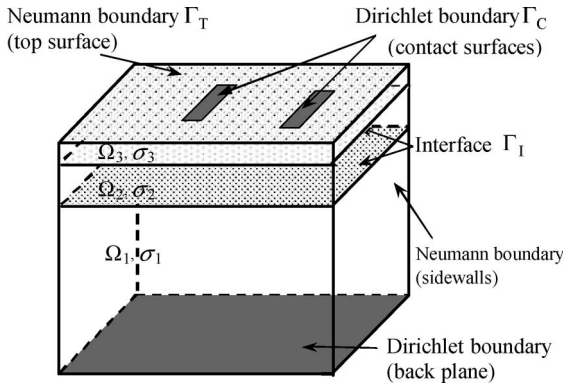

Fig. 1. Typical structure of substrate resistance extraction.

II. DBEM for Substrate Resistance Extraction

Fig. 1 shows an example of a substrate, which consists of three layers of medium regions, denoted by Ω_1, Ω_2, and Ω_3. Usually, these stratified medium regions have different height and resistivity. There are contacts on the top surface of the whole structure, which connect outer circuits. And there is also possibly a grounded plane on the very bottom. Note that the stratified structure in Fig. 1 is not always true; the example with more complex topology of medium regions will be given in Section IV-C.

For substrate resistance extraction, one contact j (called master) is set with voltage 1 V, and the other contacts 0 V. Then, the resistance R_{jk} between contact j and contact $k(k \neq j)$ can be obtained as the reciprocal of the current flowing through contact k [18]

$$\frac{1}{R_{jk}} = \int_{\Gamma_{C_k}} \sigma \cdot \frac{\partial u}{\partial n} d\Gamma = \int_{\Gamma C_k} \sigma \cdot q d\Gamma \tag{1}$$

where Γ_{C_k} is the surface of contact k, and σ is the conductivity (reciprocal of resistivity ρ). u is the electric potential, and q is the normal electric field intensity on the boundary.

If we can obtain the value of q on the contact surface, the related substrate resistances can be calculated with (1). This procedure can be repeated with setting different master contact, one by one. Finally, the full resistance matrix is obtained. We introduce the DBEM to solve the q needed in (1).

In a substrate involving multiple medium regions, the electric potential u of the steady current field fulfills the following Laplace equation in each homogenous medium region

$$\frac{\partial^2 u}{\partial x^2} + \frac{\partial^2 u}{\partial y^2} + \frac{\partial^2 u}{\partial z^2} = 0 \cdot \text{in region } \Omega_i. \tag{2}$$

With Green's identity and using the free-space Green's function as the weighting function, the Laplace (2) can be transformed into a BIE. After discretizing the region boundary into quadrilateral elements with constant interpolation, we get the discretized BIE [14]–[16], [18]

$$c_s u_s + \sum_{j=1}^{N_i} \int_{\Gamma_{ij}} q^*_{(s)} u d\Gamma = \sum_{j=1}^{N_i} \int_{\Gamma_{ij}} u^*_{(s)} q d\Gamma \text{ for region } \Omega_i \tag{3}$$

where c_s is a constant depending on the boundary geometry at the collocation point s. $u^*_{(s)}$ is the free-space Green's function related with point s, and $q^*_{(s)}$ is its normal derivative on the boundary. The entire boundary of region Ω_i is partitioned into N_i elements; Γ_{ij} represents the jth element. After calculating the boundary integrals in (3) with the efficient approach proposed in [15], a linear equation with discretized unknowns of u and q is obtained. Evaluating (3) at collocation points, one for an element in the boundary of region Ω_i, a linear equation system is formed [15]

$$\boldsymbol{H}^{(i)} \cdot \boldsymbol{u}^{(i)} = \boldsymbol{G}^{(i)} \cdot \boldsymbol{q}^{(i)} \text{ for region } \Omega_i. \tag{4}$$

Besides, u and q fulfill the compatibility equations along the interface of two adjacent medium a and b as follows:

$$\begin{cases} \sigma_a \cdot q_a = -\sigma_b \cdot q_b \\ u_a = u_b \end{cases}, \qquad \text{on interface } \Gamma_{\mathrm{I}}. \tag{5}$$

Both u and q on an interface element are unknown. We preserve u_a and q_a and represent u_b and q_b with them, or in reverse, according to (5).[1]

The matrix equations (4) for all mediums can be put together with (5). We then use the known boundary conditions (u on the contact surface is known and q on the Neumann boundaries is supposed to be zero, see Fig. 1) and reorganize the equations to form an overall linear equation system

$$\boldsymbol{A}x = \boldsymbol{b} \tag{6}$$

where unknown vector $\boldsymbol{x}$ consists of discretized unknowns of u and q, and $\boldsymbol{b}$ is a right-hand side vector corresponding to the specified voltage setting. To calculate the whole resistance network, the vector $\boldsymbol{b}$ is assigned with different values and (6) becomes a problem with multiple right-hand sides presented with

$$\boldsymbol{A}X = \boldsymbol{B}. \tag{7}$$

Here, $\boldsymbol{B}$ consists of the right-hand sides and $\boldsymbol{X}$ includes the corresponding unknown vectors. Solving this system, we can directly get q values, and in turn the resistances with (1).

From (3), we learn that only the elements on the same region's boundary have direct interaction among each other. Therefore, the matrix $\boldsymbol{A}$ in (6) and (7) becomes sparse when the simulated structure is composed of multiple regions [15]. Even so, solving the linear system (6) consumes much time, because usually above 1000 unknowns are involved. Here, we employ an efficient preconditioned generalized minimum residual (GMRES) solver [19] to solve the sparse linear equation system. Note that the organization of the sparse coefficient matrix $\boldsymbol{A}$ can affect the performance of GMRES iterative solver remarkably. For capacitance extraction with DBEM, an effective arrangement of the unknowns and collocation points, as well as the storage scheme for the matrix $\boldsymbol{A}$ has been proposed in [15]. This organization of coefficient matrix is inherited in our program for substrate resistance extraction. For more details, please refer to [15] and [20].

III. Efficient Techniques Based on DBEM

Three techniques are developed to improve the efficiency of substrate resistance extraction based on DBEM. First, we present a nonuniform boundary element partition scheme. Then, we propose a matrix reduction technology to obtain a smaller order of linear system for solution. Finally, the QMM technique is applied to make the coefficient matrix sparser and the matrix reduction much easier.

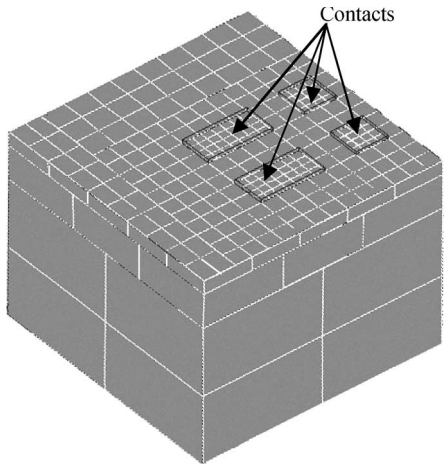

Fig. 2. Three-dimensional view of a three-layered substrate with nonuniform element mesh.

A. Nonuniform Element Partition

In DBEM simulation, the partition of boundary elements affects both computational speed and accuracy. Compared with uniform element partition, nonuniform partition involves fewer elements while preserving desirable accuracy [15]. Similar to the method for 3-D capacitance extraction [15], the substrate boundaries are partitioned with a heuristic judgment of current distribution. In this partition scheme, the current flowing directions are estimated firstly. Then, different kinds of boundary are partitioned separately, considering relevant factors. Some rules for these procedures are described as follows.

1) *Forecasting current flowing directions*: If there is no back plane, current will flow between contacts. Otherwise, some current will flow toward the back plane. However, when the layer just above the back plane has high resistivity or many contacts are close to the current injector, there will be less downward current.
2) *Dividing Dirichlet boundary*: The contact surfaces should be partitioned into much smaller elements.
3) *Dividing sidewalls*: When a sidewall surface is near to contacts, the element size should be smaller. Otherwise, it can be larger.
4) *Dividing Neumann boundary on top surface*: The element mesh should be dense where near contacts.
5) *Dividing medium interfaces*: If the layer containing the contacts is of higher resistivity than the lower layers, most current may flow downward to the back plane, and thus the interface portion just below the contacts should be partitioned into smaller elements. If the layer containing the contacts is of low resistivity, most current may flow laterally, and the entire interface between this layer and the lower layer should be partitioned into smaller elements.

This scheme is based on experience from experiments and literatures [4], [21], and may be adjusted for some complicated structures. A simple example of nonuniform element partition is shown in Fig. 2.

B. Condensing the Linear Equation System

The basic idea is to discard some u variables, since only q variables are needed to calculate the resistance with (1). Based on the unknown ordering proposed in [15], we first classify and reorder the unknowns

[1]If either σ_a/σ_b or $u^*_{(s)} = 1/(4\pi r)$ is not too small, where r is the distance between the collocation point and the integral point on the interface element, we will let $u = u_a$, $q = q_a$ for region a, and $u = u_a$ and $q = -(\sigma_a/\sigma_b)q_a$ in region b. Otherwise, we will preserve u_b and q_b and represent u_a and q_a with them. With this treatment, the coefficient of q_a (or q_b) would not be too small. This avoids a too large condition number for matrix $\boldsymbol{A}$.

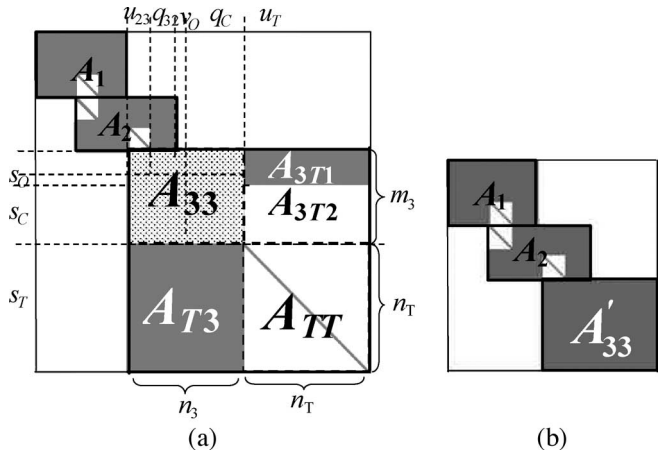

Fig. 3. Distribution of nonzero matrix entries in A for the substrate structure in Fig. 1: (a) with detailed unknown ordering and (b) after using matrix reduction technology.

for the top layer further (note that all contacts are on the top surface). Taking the structure in Fig. 1 as an example, the unknowns of type ν_{33} (both q and u unknowns in medium Ω_3 excluding those on interface) include three subtypes and can be ordered as follows:

$$\nu_o \rightarrow q_C \rightarrow U_{\mathrm{T}} \tag{8}$$

where q_c represents q unknowns on contact surfaces (Γ_{C} in Fig. 1), u_{T} denotes u unknowns on the Neumann boundary of top surface (Γ_{T} in Fig. 1), and ν_o is the other unknowns in ν_{33} (on the sidewalls). Combining the subtype permutation in (8) into the unknown ordering scheme in [15], we get the nonzero-entry distribution of coefficient matrix $\boldsymbol{A}$ for the substrate in Fig. 1, which is shown in Fig. 3(a). Only the types of collocation points and unknowns related with Ω_3 are labeled there, and they are separated by dashed lines.

Usually, the discretized unknowns related with Ω_3 account for a large part of total unknowns, as depicted in Fig. 3(a). This is because most boundary elements are located on the contacts and top surface according to the nonuniform partition. Now, consider the discretized BIEs related with Ω_3, which form the nonzero submatrices $\boldsymbol{A}_{33}$, $A_{3\mathrm{T}}(=\boldsymbol{A}_{3\mathrm{T}1} \cup \boldsymbol{A}_{3\mathrm{T}2})$, $\boldsymbol{A}_{\mathrm{T}3}$, and $\boldsymbol{A}_{\mathrm{TT}}$ in Fig. 3(a). These discretized BIEs can be expressed as the following matrix equation:

$$\begin{bmatrix} \boldsymbol{A}_{33} & \boldsymbol{A}_{3\mathrm{T}} \\ \boldsymbol{A}_{\mathrm{T}} & \boldsymbol{A}_{\mathrm{TT}} \end{bmatrix} \cdot \begin{bmatrix} \boldsymbol{x}_3 \\ \boldsymbol{u}_{\mathrm{T}} \end{bmatrix} = \begin{bmatrix} \boldsymbol{b}_3 \\ \boldsymbol{b}_{\mathrm{T}} \end{bmatrix} \tag{9}$$

where $\boldsymbol{x}_3$ is the vector consisting of unknowns u_{23}, q_{32}, ν_O, and q_C [see Fig. 3(a)]. The second row of matrix equation (9) corresponds to the equations related with the collocation points s_{T}, which are located on the top surface but not on the contacts. Therefore, coefficient matrix $\boldsymbol{A}_{\mathrm{TT}}$ is a square one. Because $\boldsymbol{u}_{\mathrm{T}}$ is useless for calculating the resistance, we can get rid of it and deduce the following matrix equation:

$$\boldsymbol{A}'_{33} \cdot \boldsymbol{x}_3 = \boldsymbol{b}'_3 \tag{10}$$

where

$$\boldsymbol{A}'_{33} = \boldsymbol{A}_{33} - \boldsymbol{A}_{3\mathrm{T}}\boldsymbol{A}_{\mathrm{TT}}^{-1}\boldsymbol{A}_{T3} \tag{11}$$

and

$$\boldsymbol{b}'_3 = \boldsymbol{b}_3 - \boldsymbol{A}_{3\mathrm{T}}\boldsymbol{A}_{\mathrm{TT}}^{-1}\boldsymbol{b}_{\mathrm{T}}. \tag{12}$$

Combining (10) with the matrix equation (4) for other medium regions, we get a new global linear equation system, whose coefficient matrix is shown in Fig. 3(b). Suppose the dimensions of matrices $\boldsymbol{A}_{33}$, $\boldsymbol{A}_{3\mathrm{T}}$, $\boldsymbol{A}_{\mathrm{T}3}$, and $\boldsymbol{A}_{\mathrm{TT}}$ in Fig. 3(a) are $m_3 \times n_3$, $m_3 \times n_{\mathrm{T}}$, $n_{\mathrm{T}} \times n_3$, and $n_{\mathrm{T}} \times n_{\mathrm{T}}$, respectively. Here, n_{T} equals to the number of elements on the Neumann boundary of top surface. m_3 equals the number of other elements in region 3, including those on contacts, sidewalls, and the interface between regions 2 and 3. n_3 is a little larger than m_3; their difference is the number of elements on the region interface. If n_{T} is large, the effect of matrix reduction in (10) becomes important, which can greatly reduce the time for solving the final global linear system.

Generally, the procedure of reduction in (11) has a computational complexity of $\boldsymbol{O}(n_{\mathrm{T}}^3 + n_{\mathrm{T}}^2 n_3 + n_{\mathrm{T}} m_3 n_3)$. We give three theorems with which the cost of above matrix reduction can be analyzed further.

Theorem 1: $\boldsymbol{A}_{\mathrm{TT}}$ is a diagonal matrix.

Proof: Consider the discretized direct BIE (3). For a s_{T}-type collocation point on the Neumann boundary of top surface (Γ_{T} in Fig. 1), the coefficient for a discretized unknown of u_{T} is

$$\int_{\Gamma_{\mathrm{T}j}} q^*_{(s_{\mathrm{T}})} d\Gamma = \int_{\Gamma_{\mathrm{T}j}} \frac{\partial u^*_{(s_{\mathrm{T}})}}{\partial \boldsymbol{n}} d\Gamma = \int_{\Gamma_{\mathrm{T}j}} \frac{-1}{4\pi r^2} \cdot \frac{\partial \boldsymbol{r}}{\partial \boldsymbol{n}} d\Gamma \tag{13}$$

where $\Gamma_{\mathrm{T}j}$ is the jth element on the top surface. r is the distance between the collocation point and the integral point on $\Gamma_{\mathrm{T}j}$, and $\boldsymbol{n}$ is the normal vector of $\Gamma_{\mathrm{T}j}$. If the collocation point is just located on $\Gamma_{\mathrm{T}j}$, the integral (13) is singular, of course not zero [15]. Otherwise, if s_{T} is not on $\Gamma_{\mathrm{T}j}$, $\partial \boldsymbol{r}/\partial \boldsymbol{n} = 0$ because vector $\boldsymbol{r}$ (within the same plane as $\Gamma_{\mathrm{T}j}$) is perpendicular to $\boldsymbol{n}$. According to Section II, the unknowns of type $\boldsymbol{u}_{\mathrm{T}}$ and collocation points of type $\boldsymbol{s}_{\mathrm{T}}$ are in the same order, and thus nonzero coefficients (i.e., the integral with collocation point just on $\Gamma_{\mathrm{T}j}$) are only on the diagonal. In other words, $\boldsymbol{A}_{\mathrm{TT}}$ is diagonal.

Theorem 2: $\boldsymbol{b}_{\mathrm{T}}$ in (9) is a zero vector.

Proof: The right-hand side $\boldsymbol{b}$ is formed by summing up all known items in (3). In the discretized BIEs for medium region 3, the only nonzero known quantity is the preset bias voltage of the master contact, whose coefficient is in the same expression of (13), except that the integral surface becomes contact surfaces. Since collocation points of type $\boldsymbol{s}_{\mathrm{T}}$ are located on the same plane with the contact, but not on the contact itself, the coefficients become always zero. Therefore, the $\boldsymbol{b}_{\mathrm{T}}$ in (9) and (12) is zero.

Theorem 3: In the discretized BIEs with collocation point of type s_{C}, the coefficients of u_{T}-type unknown is zero. In other words, the matrix $\boldsymbol{A}_{3\mathrm{T}2}$ in Fig. 3(a) is zero.

Proof: Collocation points of type s_{C} are located on contact surfaces, which are on the same plane with the elements where variables of u_{T} are located. Therefore, as analyzed in the proof of Theorem 1, the corresponding coefficient [i.e., the integral (13)] is zero. Therefore, matrix $\boldsymbol{A}_{3\mathrm{T}2}$ in Fig. 3(a) becomes a zero matrix. Also, we can say that the submatrix $\boldsymbol{A}_{3\mathrm{T}}$ is partly sparse.

These three theorems explain the distribution of nonzero matrix entries shown in Fig. 3 and are helpful to analyze the cost of our matrix reduction technology. The numbers of multiplication operations needed in (11) and (12) are:

1) $\boldsymbol{A}_{3\mathrm{T}}\boldsymbol{A}_{\mathrm{TT}}^{-1}$: Less than $m_3 \times n_{\mathrm{T}}$, because $\boldsymbol{A}_{\mathrm{TT}}$ is a diagonal matrix and $\boldsymbol{A}_{3\mathrm{T}}$ is sparse;
2) $(\boldsymbol{A}_{3\mathrm{T}}\boldsymbol{A}_{\mathrm{TT}}^{-1}) \cdot \boldsymbol{A}_{T3}$: Less than $m_3 \times n_{\mathrm{T}} \times n_3$, because $\boldsymbol{A}_{3\mathrm{T}}\boldsymbol{A}_{\mathrm{TT}}^{-1}$ has the same sparse pattern as $\boldsymbol{A}_{3\mathrm{T}}$;
3) $\boldsymbol{A}_{3\mathrm{T}}\boldsymbol{A}_{\mathrm{TT}}^{-1} \cdot \boldsymbol{b}_{\mathrm{T}}$: No operation needed, because $\boldsymbol{b}_{\mathrm{T}}$ is a zero vector.

In a word, condensing the equation system through (11) and (12) actually needs less than $m_3 \times n_{\mathrm{T}} \times (1 + n_3)$ multiplication operations. The number of addition operations is similarly bounded. The computational cost is thus much less than the aforementioned general case.

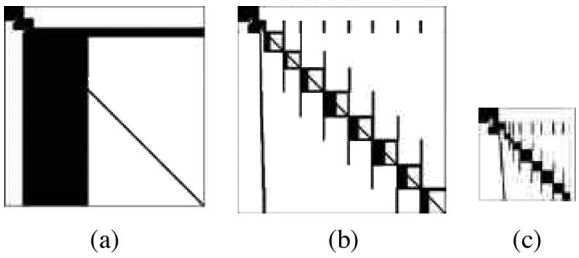

Fig. 4. Matrix population for a substrate structure similar to that in Fig. 1. (a) Original 7662 × 7662 coefficient matrix A. (b) Matrix of order 7965 after QMM cutting was applied. (c) Matrix reduced from (b), with order decreased to 3580.

For the problem of substrate resistance extraction, there are usually many contacts and all resistances among them need to be calculated. Therefore, by discarding the unknowns of type u_{T} as described, the computational time for solving (7) with multiple right-hand sides are greatly reduced. Numerical experiments verified this analysis. For example, a substrate structure with two layers involves 1511 unknowns after boundary element discretization, while only 779 unknowns remain after using the condensation technology. The condensation itself consumes only 2.20 s, but the average solving time is reduced from 3.54 to 0.48 s, for one right-hand side.

C. Applying the QMM Technique

The localization character of DBEM is revealed by (3), where the variables in each BIE are within the same medium region. This character results in a blocked sparse coefficient matrix $\boldsymbol{A}$ for a multiregion problem. A QMM method was proposed in [15] to enlarge the matrix sparsity by cutting a medium into some fictitious medium blocks. The QMM-accelerated DBEM has greatly reduced the CPU time and memory usage for interconnect capacitance/resistance extraction [15], [16].

For substrate resistance extraction, the idea of QMM can also be applied to improve the computational performance. Because there are relatively few boundary elements in the lower layers, only the top layer of substrate, which includes contacts, is decomposed into $Q_x \times Q_y$ fictitious medium blocks perpendicular to the bottom plane. Correspondingly, the nonzero submatrices for region 3 in Fig. 3(a) are replaced by many smaller nonzero submatrices. Also, the sparsity of matrix $\boldsymbol{A}$ is largely enhanced.

The matrix reduction technology in Section III-B can be easily extended to handle the system generated when QMM cutting is applied on the top layer. Then, the time of matrix reduction becomes much less than that not using QMM cutting. Taking an actual substrate structure similar to that in Fig. 1 as example, after QMM is applied ($Q_x = 4$, $Q_y = 2$), the nonzero distribution of matrix $\boldsymbol{A}$ shown in Fig. 4(a) turns into Fig. 4(b), where the original submatrix for region 3 is replaced by a sparse 8 × 8 block matrix. For the matrix in Fig. 4(b), the CPU time for matrix reduction is only 3.1 s. And then, 2.8 s are needed for the preconditioned GMRES solver to solve for one right-hand side. But if not using the QMM technique, about 580 s are needed to reduce 4492 top-surface unknowns, while solving for one right-hand side costs 10.3 s. Therefore, the QMM technique improves the computing speed of both matrix reduction and equation solution.

IV. Numerical Results

The method in this paper is implemented as SubDBEM, a program written in C++ for 3-D substrate resistance extraction. Some typical substrate structures are calculated to demonstrate the efficiency of our algorithms. All experiments are run on a Sun Fire V880 server with a frequency of 750 MHz. The first experiment is carried out on a simple structure to show the accuracy and convergence of our method. Then, SubDBEM is compared with other Green's function-based methods for a typical substrate with 52 contacts. Finally, we perform calculations for a substrate structure with lateral resistivity variation to show the versatility of SubDBEM. In the following text, all time data are in unit of second.

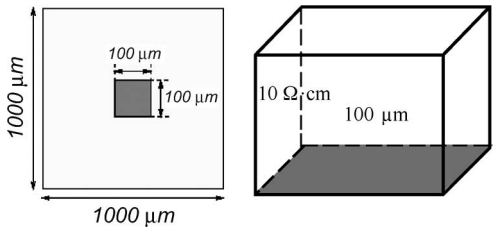

Fig. 5. Top view and 3-D view of a simple one-layer substrate structure.

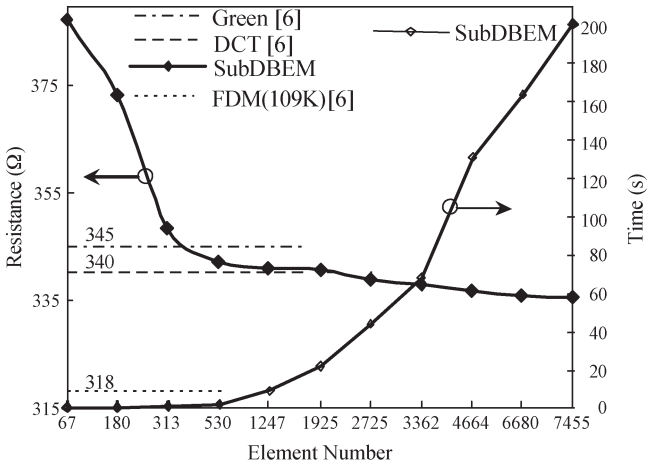

Fig. 6. Resistance value obtained by and running time of SubDBEM with different number of boundary elements.

A. Simple One-Layer Substrate

The test case is a single-layer substrate used in [6] and [10] (shown in Fig. 5). There is a contact on the center of the top surface and a grounded plane at the very bottom. The bulk height is 100 μm, and the resistivity is[2] 10 $\Omega \cdot$ cm. In [6], the contact-to-ground resistance was calculated with several methods. The computational result of the Green's function method is 345 Ω; when DCT is used for acceleration, the computed result is 340 Ω; FDM gives the converged result of 318 Ω with 109 520 mesh points [6]. With our SubDBEM, this structure is calculated for different boundary element partitions (for this simple case, the QMM technique is not used). The relationship between the element number and SubDBEM's result is depicted in Fig. 6.

From Fig. 6, we find out that as the element number becomes larger and larger, resistance decreases more and more slowly and converges finally. If we regard the value under the finest mesh (7455 elements) as criterion, the values under 67 and 530 element meshes have relative errors of 15.4% and 1.9%, respectively. At the same time, compared with the results of the Green's function method, DCT accelerated method and FDM, the converged result of SubDBEM has little discrepancy with them. The curve for computational time of SubDBEM versus element number is also drawn in Fig. 6. The time increases

[2]The resistivity given in [6] is 10 k$\Omega \cdot \mu$m, which is 1/10 of that used in [10] and our experiment. With comparing the numerical results, we find out that this may be a typo in [6]; the actual resistivity used should be 10 $\Omega \cdot$ cm.

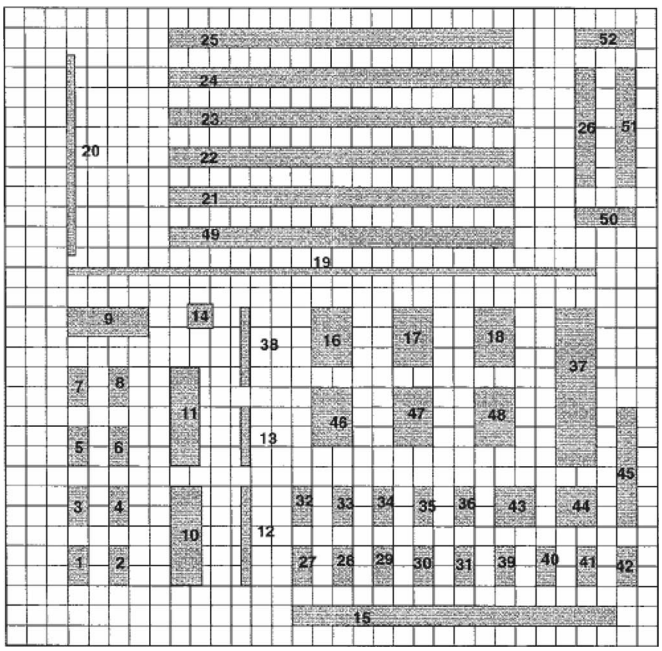

Fig. 7. Top view of a typical substrate [2].

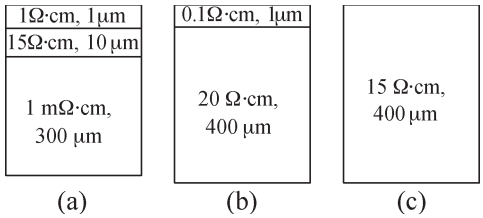

Fig. 8. Three substrate doping profiles used for extraction: (a) low-resistivity profile, (b) high-resistivity profile, and (c) singer-layer profile.

less than squarely with the element number, which can be easily seen through a log–log plot. Taking a median point for example, say which with 530 elements, the computational time of SubDBEM is 1.4 s. Its speedup ratios to the Green's function method, DCT accelerated Green's function method and FDM are about 30, 12, and 106, respectively. On an IBM RS6000 workstation (with 166-MHz frequency), the computational time of the latter three methods are 190, 76, and 674 s, respectively [6].

Although SubDBEM with dense boundary mesh gives more reliable results, we need to make balance between computational accuracy and speed. Therefore, adequate boundary meshes are used for the following experiments, which produce substrate resistance with reasonable accuracy.

B. 52-Contact Structure With Three Doping Profiles

In [2] and [10], a relatively complex structure from a mixed-signal circuit was used to demonstrate the efficiency of proposed methods for substrate resistance extraction. The example layout is a 52-contact structure on a 128×128-μm substrate, as shown in Fig. 7. Fig. 8 shows three representative kinds of doping profiles of substrate [2], [4], [10], with resistivity and height signed for each layer. In [2] and [10], the 52-contact structure with these doping profiles is calculated. We will compare their results with those from our DBEM-based method.

We first calculate resistances using a low-resistivity process, which involves three medium layers shown in Fig. 8(a). Our methods are compared with the DCT-accelerated Green's function method and the eigendecomposition-based method in [2]. They are denoted by "DCTGreen" and "EigenDec," respectively. The results of DCTGreen and EigenDec are obtained from [2]. The pure DBEM without techniques in Sections III-B and III-C (denoted by DBEM), Raphael, the famous 3-D FDM field solver of Synopsys [17], and the SubDBEM are run on the same machine to calculate this case. Table I gives the computational results of these methods, where $R_{i,j}$ means the resistance between contact i and contact j. In Table I, not all resistances are listed, like that in [2]. Because DBEM gives the same results as SubDBEM, they share a same row. For this case and the next one with high-resistivity profile, a 4×2 QMM cutting is performed on the top layer.

TABLE I
COMPUTATIONAL RESULTS FOR THE 52-CONTACT SUBSTRATE WITH LOW-RESISTIVITY PROFILE

	R_{12}	$R_{16,19}$	$R_{19,20}$	$R_{20,42}$	$R_{21,49}$	$R_{37,45}$	$R_{37,50}$
Sub DBEM /DBEM	4663	5791	6890	9.0×10^7	670	2651	89773
DCTGreen	4690	5850	6627	7.8×10^7	659	2633	89315
EigenDec	4685	5712	6643	7.8×10^7	658	2540	94327
Raphael*	4673	4341	4130	9.8×10^7	650	2476	46520

*: Set 9×10^6 grids to get converged results.

TABLE II
RELEVANT PARAMETERS FOR THE EXTRACTION OF THE EXAMPLE WITH LOW-RESISTIVITY SUBSTRATE PROFILE

	SubDBEM	QBEM	RBEM	DBEM	Raphael*	DCTGreen	EigenDec
#Unknowns	**7965**	7902	7662	7662	1.6×10^6	2647	17764
Memory (MB)	**35**	38	226	192	382	138	22.5
#GMRES Iter.	**2433**	2461	2349	2310	-	1238	1868
Time (s)	**160.4**	705	1176	4322	$>1\times10^5$	30965.5	4994.9
Workstation	Sun Ultra V880 (CPU: 750 MHz)					Sun Ultra Sparc 1	

*: The default grid setting is used in Raphael, which is 1.4×10^6 grids.

From Table I, we can see that the discrepancy between the results obtained with our method and those from [2] is within 5%, except that for $R_{20,42}$ is about 15%. Note that the reciprocal of $R_{20,42}$, i.e., the current between contacts 20 and 42 is smaller than others for several magnitudes, and the result of Raphael is close to ours (with 9% discrepancy).

Table II shows the relevant computational parameters of these methods for the low-resistivity case, which is actually the same case we used in Section III-C to explain the efficiency of applying the QMM technology (see the identity of the matrix orders in Fig. 4 and the unknown numbers in Table II). The computing time of DBEM with the condensing technique in Section III-B (denoted by RBEM) and the DBEM with the QMM technique merely (denoted by QBEM) is also listed in Table II. They show the individual impacts of these two techniques on time saving. Since we are not able to compare our method and those in [2] directly on a same computer, the relative performance of our method is only estimated ignoring the difference between processor generations. As we know, Sun Ultra Sparc 1 workstation has a CPU with frequency of 143 or 167 MHz. Therefore, Table II shows that without the techniques proposed in this paper, the pure DBEM has no advantage over either DCTGreen or EigenDec. However, SubDBEM may have a speedup of 37 to DCTGreen, and nearly 6 to EigenDec. The memory consumed by DCTGreen, EigenDec and our SubDBEM is on the same order, much less than that by Raphael or the pure DBEM.

If the high-resistivity profile in Fig. 8(b) is used, the relevant computational parameters of SubDBEM, Raphael (with default grid), DCTGreen and EigenDec for substrate extraction are listed in Table III. Since no resistance result was given in [2] for this profile,

TABLE III
RELEVANT PARAMETERS FOR THE EXTRACTION OF THE EXAMPLE WITH HIGH-RESISTIVITY SUBSTRATE PROFILE

	SubDBEM	Raphael	DCTGreen	EigenDec
#Unknowns	**7261**	8×10^5	2647	17764
Memory (MB)	**31**	209	145	26
#GMRES Iter.	**2247**	-	8030	2930
Time (s)	**112.6**	$>7\times10^4$	123630	8405.6
Workstation	Sun Ultra V880 (750 MHz)		Sun Ultra Sparc 1	

TABLE IV
COMPUTATIONAL RESULTS FOR THE 52-CONTACT SUBSTRATE WITH LOW-RESISTIVITY PROFILE

	$R_{3,4}$	$R_{10,19}$	$R_{25,50}$	$R_{33,34}$	$R_{48,50}$
SubDBEM	60.211	349.924	449.039	62.002	999.179
Method of [10]	60.352	353.551	437.771	61.921	1005.637
IE3D	61.333	365.343	450.343	62.734	1020.987
Raphael*	52.960	244.861	371.576	56.302	759.842

*: Set 6×10^6 grids to get converged results.

we focus on the performance comparison. The data of DCTGreen and EigenDec are got on Sun Ultra Sparc 1 [2]. Assuming the CPU used in [2] has frequency of 143 MHz, our SubDBEM is more than 200 times faster than the DCTGreen and 14 times faster than the EigenDec. While considering the memory usage, the SubDBEM is much superior to the DCTGreen, but consumes a little more than the EigenDec.

Compared with those in Table II, the DCTGreen and EigenDec consume more CPU time for the example with high-resistivity profile. This is because the number of GMRES iterations increases a lot in calculating the high-resistivity example. However, SubDBEM performs better for the substrate with high-resistivity profile than the one with low-resistivity profile. The main reason is that in the former there is only one medium interface rather than two interfaces in the latter. This reduces the total number of boundary elements. Besides, the number of GMRES iterations also reduces for the high-resistivity example.

For the 52-contact substrate with single-layer profile in Fig. 8(c), no computational result was given in [2]. But this structure was discussed in [10], where a fast-convergent Green's function and an analytical solution for the double surface integrals of substrate resistance extraction were proposed. We will compare the computational results of SubDBEM with those from [10]. To use the QMM technique in SubDBEM, the substrate is first cut into two layers (with heights 20 and 380 μm, respectively), and then the top layer is cut into 2×4 parts.

In Table IV, some mutual resistances computed by SubDBEM are listed, along with corresponding results of Raphael, and those from [10]. IE3-D is a 3-D full-wave, method of moment (MOM), integral equation electromagnetic simulator, whose computational results are got from [10]. From the table, we can see that the error of SubDBEM is less than 5% (if considering results of IE3-D as the standard), and SubDBEM has similar accuracy as the method in [10]. But the accuracy of Raphael is much worse for this example. The CPU time of SubDBEM is only 51.7 s on calculating all the resistances. It is more than 940 times faster than IE3-D, which consumes up to 73 364 s on a PC with 500-MHz frequency [10]. On a Sun Ultra 12 workstation, the method with analytical Green's function costs 441.2 s to complete the resistance extraction [10]. Although we have no exact data of the working frequency of Sun Ultra 12 workstation, we learn that it will be above 140 MHz, from the website of SUN, Inc. Then, SubDBEM is even a bit faster than the analytical method in [10]. Moreover, an important advantage of our method over the method of [10] is that the former can handle substrates with arbitrary doping profiles, while the latter only handles structures with one or two stratified medium layers.

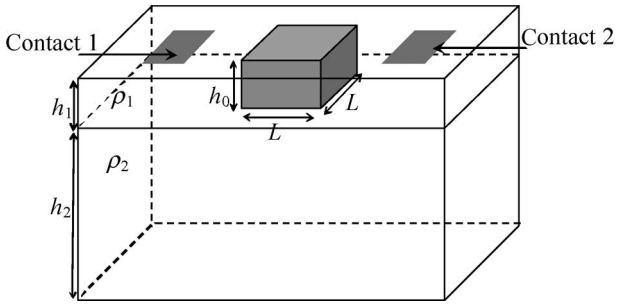

Fig. 9. Substrate with lateral resistivity variation.

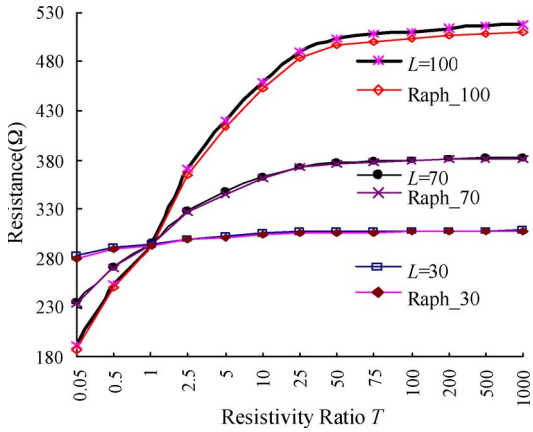

Fig. 10. Resistance obtained with SubDBEM and Raphael, varied with the resistivity of lateral variation region.

C. Structure With Lateral Resistivity Variation

In most literatures of substrate resistance extraction, the stratified structures are calculated as example, partially because that the Green's function cannot be deduced for substrates with complicated doping profiles. On the contrary, the DBEM in Section II has no limitation on the topology of mediums in a substrate. To demonstrate this advantage of DBEM over the Green's function-based methods, a structure with lateral resistivity variation (shown in Fig. 9) is calculated.

This case has two medium layers, with resistivities $\rho_1 = 0.1\ \Omega\cdot$cm and $\rho_2 = 35\ \Omega\cdot$cm, respectively. The height of upper layer is $h_1 = 5\ \mu$m, and the height of lower layer is $h_2 = 400\ \mu$m. In the center of upper layer, there is an $L\times L$ square region with different resistivity, which is T times of ρ_1. The height of this resistivity variation region is $h_0 = 5\ \mu$m. The dimension of whole structure is $200\times200\ \mu$m. On the top surface, there are two 10×10-μm contacts located to the left and right sides of the resistivity variation region. The resistance between these two contacts is calculated with different values of L and T. For $L = 100$, 70, or 30 μm, the resistances calculated by SubDBEM and Raphael are depicted as curves in Fig. 10, with the resistivity ratio T varied. In SubDBEM, 3×3 QMM cutting is performed for the top layer so as to make the resistivity-variation region be the central fictitious region.

We can learn from the figure that the results of SubDBEM are very close to Raphael, illustrating the high accuracy of our method for such complicated case. At the same time, the speedup ratio of SubDEBM to Raphael with default grid is about 818.8/17.5 = 47. Besides, the resistance increases with the resistivity of the lateral variation region, and finally converges. This is because the block region behaves more and more like an obstacle in the path of current flow as its resistivity gets larger and larger. When the resistivity is large enough, the current will not flow through this region at all, so the resistance between two

contacts reaches a converged value. Also, the resistance increases more quickly for larger L. This can be explained similarly, because the larger the resistivity-variation region, the more it influences the current flow.

V. Conclusion

In this paper, the DBEM is presented to extract 3-D substrate resistance for the first time. Different from the Green's function-based methods, only the free-space Green's function is used in DBEM. Therefore, DBEM is able to handle substrate structure with arbitrary doping profiles, which overcomes the limitation of existing Green's function-based methods. However, DBEM discretizes the entire boundary of a substrate region and produces more unknowns than the Green's function method. To improve the performance of DBEM, three efficient techniques are proposed for substrate resistance extraction. With nonuniform element partition, the technique of condensing the linear equation system, the number of unknowns in DBEM is greatly reduced. Also, with the enhanced sparsity brought by the QMM approach, the equation reduction and final equation solution can be performed much faster. The combination of these techniques largely improves the computational efficiency of the DBEM, especially for the structure involving many contacts and lateral resistivity variation.

Numerical results demonstrate high accuracy of our DBEM-based method. The experiments on a typical 52-contact substrate structure show that our method is several times faster than the Green's function method, which is accelerated by the eigendecomposition technique and tens of times faster than the DCT-accelerated Green's function method. An example with lateral resistivity variation is also simulated to show the versatility of our method.

References

[1] R. Gharpureys and E. Charbon, "Substrate coupling: Modeling, simulation and design perspectives," in *Proc. 5th Int. Symp. Quality Electron. Des.*, Mar. 2004, pp. 283–290.

[2] J. P. Costa, M. Chou, and L. M. Silveira, "Efficient techniques for accurate modeling and simulation of substrate coupling in mixed-signal IC's," *IEEE Trans. Comput.-Aided Design Integr. Circuits Syst.*, vol. 18, no. 5, pp. 597–607, May 1999.

[3] T. Smedes, N. P. van der Meijs, and A. J. van Genderen, "Extraction of circuit models for substrate cross-talks," in *Proc. ACM/IEEE Int. Conf. Comput.-Aided Des.*, Nov. 1995, pp. 199–206.

[4] N. Masoumi, M. I. Elmasry, and S. Safavi-Naeini, "Fast and efficient parametric modeling of contact-to-substrate coupling," *IEEE Trans. Comput.-Aided Design Integr. Circuits Syst.*, vol. 19, no. 11, pp. 1282–1292, Nov. 2000.

[5] N. K. Verghese and D. J. Allstot, "Rapid simulation of substrate coupling effects in mixed-mode ICs," in *Proc. IEEE Custom Integr. Circuits Conf.*, May 1993, pp. 18.3.1–18.3.4.

[6] R. Ghapurey and R. G. Meyer, "Analysis and simulation of substrate coupling in integrated circuits," *Int. J. Circuit Theory Appl.*, vol. 23, no. 4, pp. 381–394, Jul./Aug. 1995.

[7] A. M. Niknejad, R. Gharpurey, and R. G. Meyer, "Numerically stable Green function for modeling and analysis of substrate coupling in integrated circuits," *IEEE Trans. Comput.-Aided Design Integr. Circuits Syst.*, vol. 17, no. 4, pp. 305–315, Apr. 1998.

[8] C. Xu, T. Fiez, and K. Mayaram, "On the numerical stability of Greens function for substrate coupling in integrated circuits," *IEEE Trans. Comput.-Aided Design Integr. Circuits Syst.*, vol. 24, no. 4, pp. 653–658, Apr. 2005.

[9] R. Gharpurey, "Modeling and analysis of substrate coupling in integrated circuits," Ph.D. dissertation, Univ. California, Berkeley, CA, 1995.

[10] N. Masoumi, M. I. Elmasry, S. Safavi-Naeini, and H. Hadi, "A novel analytical model for evaluation of substrate crosstalk in VLSI circuits," in *Proc. 1st IEEE Int. Workshop Electron. Des., Test and Appl.*, Jan. 2002, pp. 355–359.

[11] E. Schrik and N. R. van der Meijs, "Combined BEM/FEM substrate resistance modeling," in *Proc. IEEE/ACM Des. Autom. Conf.*, Jun. 2002, pp. 771–776.

[12] S. Donnay and G. Gielen, *Substrate Noise Coupling in Mixed-Signal ASICs*. Boston, MA: Kluwer, 2003.

[13] S. Ardalan and M. Sachdev, "An overview of substrate noise reduction techniques," in *Proc. 5th Int. Symp. Quality Electron. Des.*, Mar. 2004, pp. 291–296.

[14] C. A. Brebbia, *The Boundary Element Method for Engineers*. London, U.K.: Pentech, 1978.

[15] W. Yu, Z. Wang, and J. Gu, "Fast capacitance extraction of actual 3-D VLSI interconnects using quasi-multiple medium accelerated BEM," *IEEE Trans. Microw. Theory Tech.*, vol. 51, no. 1, pp. 109–199, Jan. 2003.

[16] X. Wang, D. Liu, W. Yu, and Z. Wang, "Improved boundary element method for fast 3-D interconnect resistance extraction," *IEICE Trans. Electron.*, vol. e88-c, no. 2, pp. 232–240, Feb. 2005.

[17] Synopsys Corp., *Raphael Reference Manual*, 2000.

[18] Z. Wang and Q. Wu, "A two-dimensional resistance simulator using the boundary element method," *IEEE Trans. Comput.-Aided Design Integr. Circuits Syst.*, vol. 11, no. 4, pp. 497–504, Apr. 1992.

[19] W. Yu and Z. Wang, "Enhanced QMM-BEM solver for three-dimensional multiple-dielectric capacitance extraction within the finite domain," *IEEE Trans. Microw. Theory Tech.*, vol. 52, no. 2, pp. 560–566, Feb. 2004.

[20] W. Yu, Z. Wang, and X. Hong, "Preconditioned multi-zone boundary element analysis for fast 3-D electric simulation," *Eng. Anal. Bound. Elem.*, vol. 28, no. 9, pp. 1035–1044, Sep. 2004.

[21] D. K. Su, M. J. Loinaz, S. Masui, and B. A. Wooley, "Experimental results and modeling techniques for substrate noise in mixed-signal integrated circuits," *IEEE J. Solid-State Circuits*, vol. 28, no. 4, pp. 420–430, May 1993.

Comments on "Modeling of Metallic Carbon-Nanotube Interconnects for Circuit Simulations and a Comparison With Cu Interconnects for Sealed Technologies"

Hong Li, Wen-Yan Yin, and Jun-Fa Mao

I. Introduction

In [1], Raychowdhury and Roy proposed a compact resistance, inductance, and capacitance circuit model for the metallic single-walled carbon nanotube (CNT) interconnects, in which the CNT's differential resistance was given as follows:

For low biases $(V < V_{\text{critical}})$

$$R_{\text{diff}}^{\text{low}} = \frac{dV}{dI} = \left(\frac{h}{4e^2}\right)\Theta\left(\frac{l}{\lambda_{\text{low}}}\right). \tag{1}$$

For high biases $(V > V_{\text{critical}})$

$$R_{\text{diff}}^{\text{high}} = \frac{dV}{dI} = \left(\frac{h}{4e^2}\right)\Theta\left(\frac{l}{\lambda_{\text{low}}} + \frac{l}{\frac{0.16l}{V} + \lambda_{\text{high}}}\right) \tag{2}$$

where

$$\Theta(x) = \begin{cases} 1, & x < 1 \\ x, & \text{otherwise} \end{cases} \tag{3}$$

and h is the Plank's constant, e is the electronic charge, and λ is the mean free path (mfp). As given in [1], $V_{\text{critical}} = 160$ mV and $\lambda_{\text{high}} \approx 30$ nm, while λ_{low} is in the range of 1.0 and 1.6 μm.

Manuscript received January 17, 2006; revised May 17, 2006. This paper was recommended by Associate Editor D. Sylvester.

The authors are with the Center for Microwave and RF Technologies, Shanghai Jiao Tong University, Shanghai 200240, China (e-mail: lihong@sjtu.edu.cn; wyyin@sjtu.edu.cn; jfmao@sjtu.edu.cn).

Digital Object Identifier 10.1109/TCAD.2006.883920